npj | climate and atmospheric science

Article

Published in partnership with CECCR at King Abdulaziz University

https://doi.org/10.1038/s41612-024-00706-1

Role of Pacific Ocean climate in regulating runoff in the source areas of water transfer projects on the Pacific Rim

Check for updates

Feng Chen [1,2], Shijie Wang [1,2], Qianjin Dong [3], Jan Esper [4,5], Ulf Büntgen [5,6,7], David Meko [8], Hans W. Linderholm [9], Tao Wang [10], Weipeng Yue [1], Xiaoen Zhao [1,2], Martín Hadad [11], Álvaro González-Reyes [12] & Fahu Chen [13,14,15]

Over the past two decades, more frequent and intense climate events have seriously threatened the operation of water transfer projects in the Pacific Rim region. However, the role of climatic change in driving runoff variations in the water source areas of these projects is unclear. We used tree-ring data to reconstruct changes in the runoff of the Hanjiang River since 1580 CE representing an important water source area for China's south-north water transfer project. Comparisons with hydroclimatic reconstructions for the southwestern United States and central Chile indicated that the Pacific Rim region has experienced multiple coinciding droughts related to ENSO activity. Climate simulations indicate an increased likelihood of drought occurrence in the Pacific Rim region in the coming decades. The combination of warming-induced drought stresses with dynamic El Niño (warming ENSO) patterns is a thread to urban agglomerations and agricultural regions that rely on water transfer projects along the Pacific Rim.

Due to the imbalance between the distribution of water resources and regional economic development, many water-transfer projects have been developed on the Pacific Rim that have substantially affected the landscape and human and ecological communities. Prominent examples include China's south–north water transfer project and the California water transfer project[1–4]. However, during the past 20 years, along with increased global warming, there has been a significant increase in drought frequency in the water source areas of these water transfer projects. The resulting large reduction in runoff has threatened the water security of the many urban agglomerations that depend on transferred water[1,5–8]. As the main water source of China's south–north water transfer project, the runoff of the Yangtze and Hanjiang rivers has undergone decreasing trends over the past ~40 years. In particular, an extreme drought occurred in the Yangtze River Basin in June 2022, where the surface areas of water bodies significantly decreased, causing major national-scale impacts[7,9,10]. Simultaneously, the western coasts of North and South America have experienced increased droughts over the past ~20 years[11–13]. The continuing decrease in runoff in all these source regions caused excessive groundwater pumping and gradually depleting the water reservoirs accessible for industrial, agricultural, and domestic consumption[11,14–17]. The occurrence of mega-droughts accelerates regional-to-large-scale forest degradation, increases the frequency and severity of wildfires, and sustainedly damages aquatic ecosystems[18–22]. The affected regions include some of the world's most important irrigation agriculture and industrial areas along the Pacific Rim,

[1]Yunnan Key Laboratory of International Rivers and Transboundary Eco-Security, Institute of International Rivers and Eco-Security, Yunnan University, Kunming, China. [2]Southwest United Graduate School, Kunming, China. [3]State Key Laboratory of Water Resources Engineering and Management, Wuhan University, Wuhan, China. [4]Department of Geography, Johannes Gutenberg University, Mainz, Germany. [5]Global Change Research Institute (CzechGlobe), Czech Academy of Sciences, Brno, Czech Republic. [6]Department of Geography, University of Cambridge, Cambridge, UK. [7]Department of Geography, Masaryk University, Brno, Czech Republic. [8]Laboratory of Tree-Ring Research, University of Arizona, Tucson, AZ, USA. [9]Regional Climate Group, Department of Earth Sciences, University of Gothenburg, Gothenburg, Sweden. [10]Climate Change Research Center and Nansen-Zhu International Research Centre, Institute of Atmospheric Physics, Chinese Academy of Sciences (CAS), Beijing, China. [11]Laboratorio de Dendrocronología de Zonas Áridas CIGEOBIO (CONICET-UNSJ), San Juan, Argentina. [12]Instituto de Ciencias de la Tierra, Facultad de Ciencias, Universidad Austral de Chile, Valdivia, Chile. [13]Key Laboratory of Alpine Ecology, CAS Center for Excellence in Tibetan Plateau Earth Sciences and Institute of Tibetan Plateau Research, Chinese Academy of Sciences (CAS), Beijing, China. [14]Key Laboratory of Western China's Environmental Systems (Ministry of Education), College of Earth and Environmental Sciences, Lanzhou University, Lanzhou, China. [15]State Key Laboratory of Earth Surface Processes and Resource Ecology, Faculty of Geographical Science, Beijing Normal University, Beijing, China.
e-mail: feng653@163.com

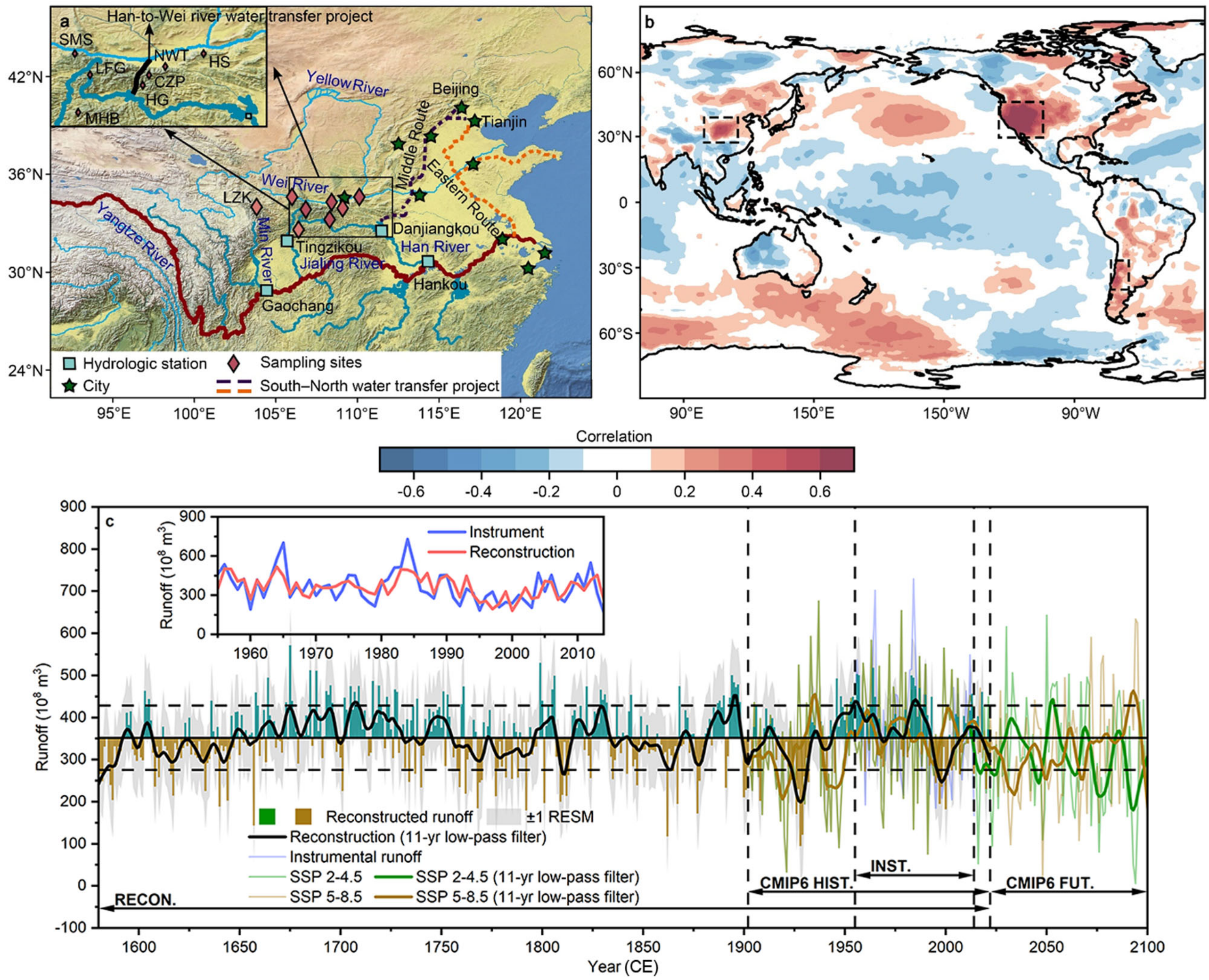

Fig. 1 | Spatio-temporal characteristics of the runoff reconstruction. **a** Map showing the locations of tree-ring sites and hydrological stations. Also shown are the routes related to the Hanjiang River. **b** This study, along with reconstructions from the southwestern United States[5] and Central Chile[25], corresponds to the spatial correlation patterns (1955–2014) of gridded August–July PDSI respectively in Asia, North America, and South America. Correlations between the runoff reconstruction in Hanjiang River and sea surface temperatures are also shown. **c** Reconstructed runoff in Hanjiang River from 1580 to 2022 CE, together with the 11-year low-pass filtered reconstruction, highlighting multi-decadal variability. Inset shows actual versus estimated August–July runoff during the instrumental period. The runoff variation from the downscaled and bias-corrected multi-model CMIP6 SSP2-4.5 and SSP5-8.5 ensemble (24 models; Supplementary Table 5) during both the 'historical' (1902–2014 CE) and 'future' (2015–2100 CE) simulation periods of these runs are also shown.

and the increased frequency of megadroughts affects global supply chains[5,6].

Megadroughts on the western coasts of North and South America have been linked to climate forcings, where co-occurring hydroclimate fluctuations can partially be explained by changes in the Pacific Ocean[5,12,23–25]. There is also evidence of coherence among runoff-sensitive proxies on the western coasts of North and South America and the El Niño-Southern Oscillation (ENSO)[26–31]. Moreover, hydroclimate reconstructions have indicated an out-of-phase relationship between drought in North America and Monsoonal Asia[32], and climate change in the Pacific Ocean region has been linked to runoff fluctuations in Monsoonal Asia[33,34]. Taken together, these evidences imply the existence of anomalous ENSO-induced runoff and hydroclimatic patterns, which may affect the operation of water transfer projects on the Pacific Rim. Despite the progress made in characterizing runoff variations and their causes in the source areas of the water transfer projects of North and South America[26–31], little is understood about the long-term runoff characteristics of China's mega south-north water transfer project, and their potential association with runoff variations on the western coasts of North and South America. Here, we present an annual-resolution runoff reconstruction for the Hanjiang River since 1580 CE, along the central route of China's south-north water transfer project (Fig. 1). This new runoff record enables us to place the 60-year measured and 100-year projected runoff variations within a multi-centennial perspective, and to explore the linkages between hydroclimate variations in the source areas of water transfer projects on the Pacific Rim. We then use multi-model ensemble runoff projection from the Coupled Model Intercomparison Project 6 (CMIP6) to place regional and inter-regional droughts in the context of past hydroclimate variations and projected future changes driven by global warming.

Results and discussion

Runoff reconstruction for the Hanjiang river

We developed runoff-sensitive tree-ring-width chronologies from pine trees growing at sites with shallow rocky soils in the Qinling Mountains of central China (Fig. 1a and Supplementary Fig. 1 and Table 1). These records were used to reconstruct August–July runoff for the Hanjiang River (Danjiangkou) with annual resolution from 1580 to 2022 CE, using nested principal component regression (see Methods).

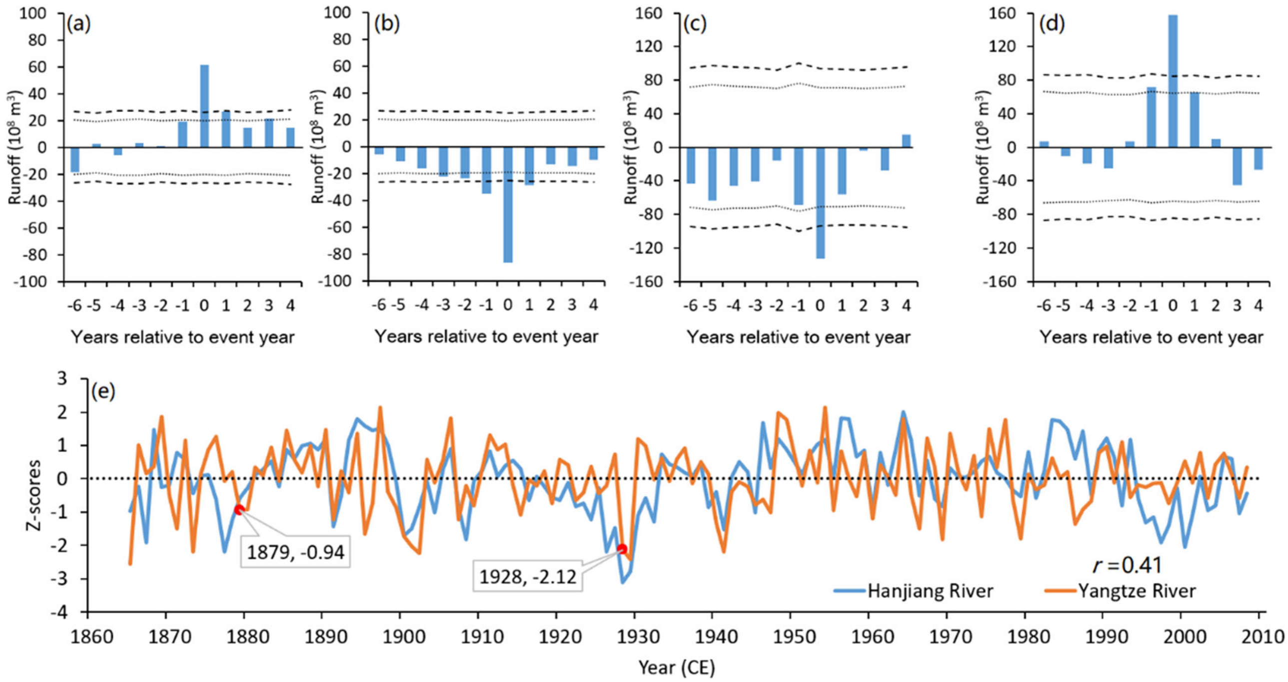

Fig. 2 | Runoff characteristics during documented drought and flood events. **a** Results of the superposed epoch analysis (SEA) of the runoff reconstruction in the Hanjiang River for 57 historical floods during 1580–1955 CE, **b** 54 historical droughts during 1580–1955 CE, **c** 13 instrumental droughts during 1955–2014 CE, and **d** 14 instrumental floods during 1955–2014 CE. Dashed and dotted lines mark 99% and 95% significance. **e** The runoff reconstruction in the Hanjiang River based on tree rings shown together with the observed Yangtze river runoff data.

The reconstructions passed all calibration and verification tests and explains 40.7–44.8% of the instrumental runoff variance during the 1955–2014 calibration period (Supplementary Fig. 2 and Table 2). Low runoff periods occurred during 1580–1592, 1607–1647, 1757–1796, 1842–1869, 1872-1881, 1900–1909, 1916–1943, and 1993–2007; while high runoff periods occurred during 1659–1732, 1741–1756, 1797–1806, 1815–1835, 1882–1899, 1944–1992, and 2008–2017 (Fig. 1c). Overall lowest runoff was reconstructed from 1916–1943 and recently from 1993–2007 during periods when Hanjiang runoff fell below 262.8×10^8 and 267.6×10^8 m^3, respectively. The reduced runoff in 2022, 68.5×10^8 m^3 below the long-term mean (351.7×10^8 m^3) largely originates from the severe drought in the Yangtze River basin[9].

Our runoff reconstruction includes 54 extreme flood and 57 extreme drought events documented in historical literature in the Hanjiang River basin and surrounding areas before 1950 CE[35] (Supplementary Table 3). Our reconstruction effectively captures the extreme runoff generated by anomalous droughts and floods, especially the lowest runoff (94.3×10^8 m^3) during the past 443 years caused by the 1928 extreme drought event in northern China. By comparing the new reconstruction with documented floods, we find the runoff estimates were significantly higher (61.2×10^8 m^3, $p < 0.01$) than would be expected by chance. Additionally, runoff decreased by more than 1 standard deviation (86.4×10^8 m^3) in the reconstruction during the 57 historical drought years, and a statistically significant reduction ($p < 0.01$) occurred two years before and after these historical drought years (Fig. 2a, b).

It is noteworthy that these linkages between our reconstruction and the historical records are much stronger during the instrumental period. The Superposed Epoch Analysis (SEA) of the flood and drought years after 1949 do not show more significant high/low runoff conditions (Fig. 2c, d), but the 13 droughts and 14 floods occurred during the instrumental period of 1955–2014, occupying about 50% of the time. The frequency and amplitude of droughts and flood increased significantly compared to the pre-instrumental period, particularly for the extreme floods. The occurrence of this asymmetric response proves that there are some flaws in the ability of tree rings to record extreme floods, and strong changes in the external environment due to global warming[36,37]. Therefore, more cross verifications of tree-ring chronologies or other proxy data are needed to accurately capture extreme floods and droughts. Our runoff reconstruction also correlates significantly ($r = 0.41$, $p < 0.01$) with the Yangtze River runoff at Hankou station, which has the longest observed runoff record (1865–2008) for southern China (Fig. 2e). This association implies that the low runoff of the Yangtze River is significantly affected by drought in northern China, such as during 1876–1879 and 1928.

Teleconnections between complex drought events in the Pacific Rim and SST conditions in the Pacific Ocean

A comparison of our runoff reconstruction with hydroclimate reconstructions from the southwestern United States[5] and Central Chile[25] shows that all these records correlate well with instrumental PDSI[38] and runoff data[39] (Supplementary Figs. 3–6). Localized hydrologic cycles dominate runoff changes, yet there may still be common drivers that lead to synergistic changes across the three regions, especially with sustained consistency in recent decades (Supplementary Fig. 7). The Paleo Hydrodynamics Data Assimilation product (PHYDA)[40] reasonably reproduces regional hydrologic variations (Supplementary Fig. 8a), as dry and wet variations on land dominated by tree-ring width data are revealed. Thus, predominant El Niño patterns are shown during anomalous dry periods in the Hanjiang River basin, whereas the southwestern United States and Central Chile appear to be associated with cool, La Niña-like Pacific SST patterns[12] (Supplementary Fig. 9a–c).

Warm SST anomalies are particularly obvious in the Central Pacific during when Hanjiang River drought conditions were out of phase/disconnected from the conditions in southwestern United States and Central Chile (Supplementary Fig. 9d–f). These periods coincide with El Niño patterns and neutral SST conditions in the Atlantic (Fig. 3a). When drought conditions are common to all three regions, the unsynchronized reactions of SSTs in the eastern and western Central Pacific occur (Supplementary Fig. 9g–i). Under the conditions of warm SST anomalies in the western Central Pacific that caused the Hanjiang River droughts, cold anomalies in the eastern SST showing an inversion accompanied the droughts in the

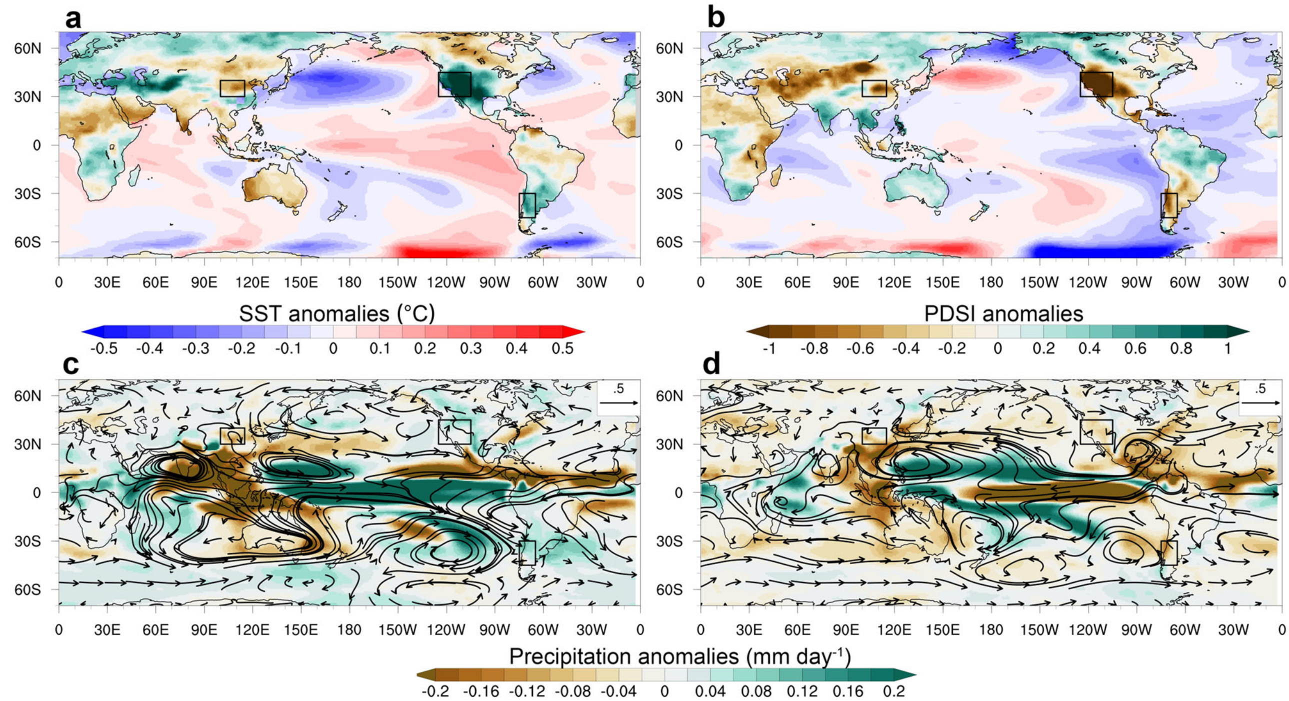

Fig. 3 | Relationship between hydroclimate variations on the Pacific Rim and Pacific Ocean climate variability. **a** Composites of SST and PDSI from PHYDA[40] for all the years corresponding to drought conditions in Hanjiang River and wet conditions in the southwestern United States[5] and Central Chile[25]. **b** Composites of SST and PDSI from PHYDA for all the years corresponding to drought conditions in all three regions. PDSI and SST data are anomalies with respect to the period of 1580–2000. **c** Composites of precipitation and 850 hPa water vapor transport anomalies (vectors, where uq and vq are multiplied by 1000) in the CESM-LME[65,66] for all the years corresponding to the medium ELI[42,43] conditions. Precipitation and water vapor data are anomalies with respect to the period of 1580–2005. **d** Analogous composites for the low ELI conditions.

southwestern United States and Central Chile (Fig. 3b). As discussed above, moisture conditions in the water source areas of the water transfer projects in the Pacific Rim region are related to the ENSO longitudinal dynamics-dominated climate.

The inconsistencies between simulations and reconstructions on interannual scales suggest the potential influences of internal variabilities[41] (Supplementary Fig. 8b), while the ENSO longitudinal dynamics-dominated patterns shown in Fig. 3 are supported by the map of the composite 850 hPa water vapor flux and precipitation rate in different categories of the ENSO Longitude Index (ELI)[42,43], implying the occurrence of El Niño at different longitudes. Accompanying the overall warm ENSO phase (medium ELI), the SST anomaly was negative in the North Pacific and positive in the equatorial central Pacific. The Pacific Walker circulation and zonal winds were relatively weak, when anomalously strong westerly moisture flux anomalies were generated in the equatorial central Pacific Ocean. This configuration may lead to a decrease in water vapor transport from the equatorial Pacific to eastern China, causing the rain belt to move southward. Anomalous north-westerly winds over central-northern China reduced the supply of oceanic water vapor to this region. This in turn results in drought conditions in the Hanjiang River basin[44–47] (Fig. 3a, c and Supplementary Fig. 10a). Additionally, the anomalous westerly anomalies in the equatorial Pacific enhance the water vapor transport from the Pacific Ocean to North and South America, bringing more abundant precipitation to regions such as the southwestern United States and Central Chile[12,48–50].

When El Niño occurs in the western Central Pacific (low ELI), it is accompanied by inverse cold SST anomalies in the equatorial eastern Pacific. Anomalous cooling causes an increase in sea level pressure, resulting in a zonal easterly anomaly that intersects the westerly anomaly in the western Pacific (Fig. 3b, d and Supplementary Fig. 10b). At the same time, eastern Asia, southwestern North America, and South America all show a pattern of water vapor transport from continent to ocean, with linked droughts occurring within these three regions. The extent of runoff changes in the reconstruction and CESM-LME similarly support the above result that differences in the occurrence positions of El Niño influence the occurrence of reverse and synergistic droughts in the Pacific Rim (Supplementary Fig. 11). Taken together, these results suggest an asynchronous linkage in response to Central Pacific SST between runoff on the eastern and western coasts of the Pacific Ocean under normal conditions. However, the occurrence of synchronous cold SST anomalies in the eastern equatorial Pacific and North Pacific, accompanied by a warm SST anomaly in the western equatorial Pacific, caused linked and devastating droughts in Hanjiang River, the southwestern United States, and Central Chile.

Future runoff projections

Using the downscaled and bias-corrected projections of the ensemble of 24 CMIP6 climate models (see Methods), we found a predominantly fluctuating change from 1955 to 2014 CE, accompanied by an insignificant downward trend (Fig. 1c). Future predictions of the multi-model ensemble runoff indicate a large decrease (−15.84% for SSP2-4.5 and −12.10% for SSP5-8.5) in runoff relative to the instrumental mean that is expected to persist until the end of the 21st century (Fig. 4a, b and Supplementary Fig. 13). We find that the projected distribution of runoff and the horizontal line representing the mean during the period of 2070 to 2100 CE imply a large decline in projected runoff in the SSP2-4.5 scenario, but a recovery in projected runoff in the SSP5-8.5 scenario, which is still lower than the historical mean (Supplementary Fig. 14). Under the two future scenarios, the southwestern United States runoff first experiences ~20 years of decline and then continues to rise until the end of the 21st century when it increases by 2.59% and 5.97%. Central Chilean runoff, on the other hand, experienced a short recovery and then a sharp decline until the 2060 s, followed by more drastic changes in both scenarios in reverse, especially with a 39.18% decrease until the end of the 21st century in the SSP5-8.5 scenario (Fig. 4b and Supplementary Figs. 13 and 14).

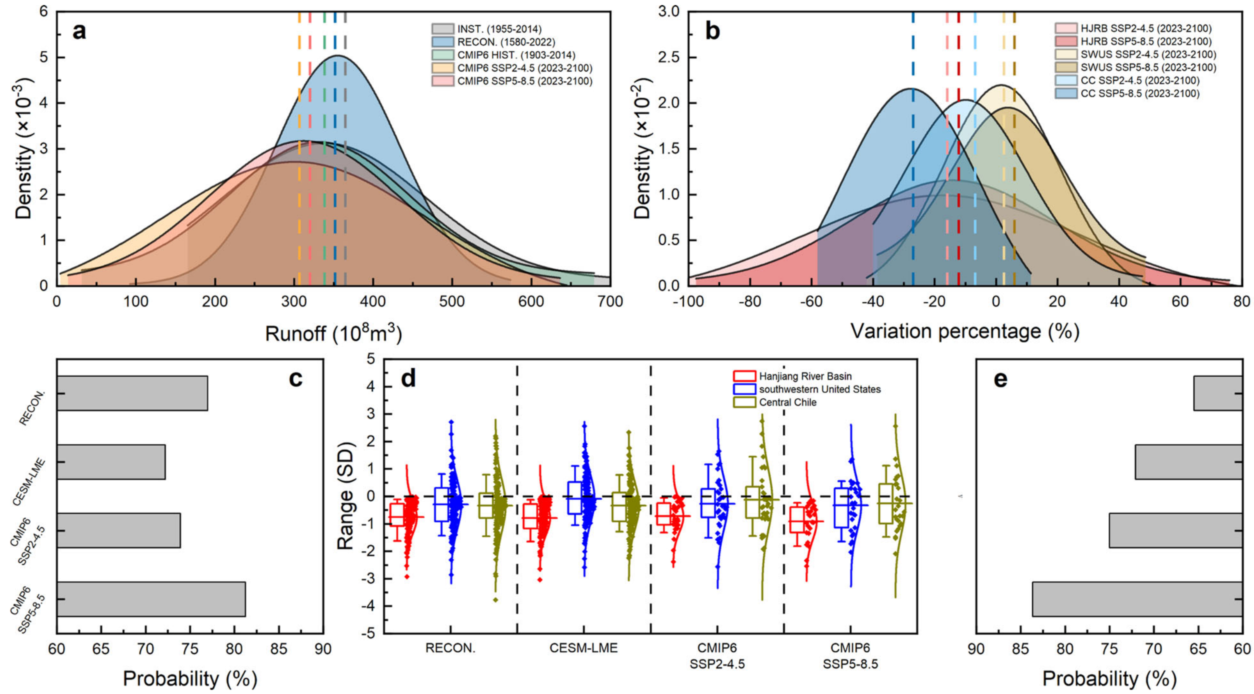

Fig. 4 | CMIP6 projections of hydroclimate variations of the Hanjiang River in China, southwestern United States, and Central Chile. **a** Kernel density profiles of the runoff reconstruction, instrumental period, CMIP6 projections in the Hanjiang River. **b** Future runoff variations of the Hanjiang River Basin (HJRB), southwestern United States (SWUS) and Central Chile (CC) during the period of 2023–2100 under SSP2-4.5 and SSP5-8.5 scenarios. The vertical dashed lines represent the respective mean values. **c** The probabilities of at least one of the other two regions experiencing drought under the Hanjiang River drought conditions in the reconstruction, CESM-LME, and CMIP6 future scenarios. **d** Box-and-whisker plots of runoff changes in the Hanjiang River Basin, the southwestern United States, and Central Chile for the years involved in **c**. Here, the box of the box-and-whisker plot indicates the 25–75% range, the whisker line indicates the 10–90% range, and the middle line indicates the mean. The scatter and normal distribution curves are given in parallel. Here all runoff data are first-order differenced and the variation ranges are indicated using multiples relative to the standard deviation (SD). **e** The probabilities of low and medium ELI conditions under all El Niño occurrence in the reconstruction, CESM-LME, and CMIP6 future scenarios.

As a result of global warming, the hydroclimate in the Pacific Rim has changed dramatically. Under future drought conditions in the Hanjiang River, the probabilities of at least one of the southwestern United States and Central Chile also experiencing droughts have risen compared to the historical period. In particular, under the SSP5-8.5 scenario, the frequency of compound droughts increases by 9.03% and 4.25% compared to the CESM-LME and the reconstruction, respectively, accompanied by more severe drought levels compared to the SSP2-4.5 scenario (Fig. 4c, d). We find that under the whole El Niño conditions, the probability of the future El Niño occurring in the western or central Pacific will increase, rather than in the eastern Pacific. The probabilities would rise by 2.54% and 9.53% in the SSP2-4.5 scenario compared to CESM-LME and the reconstruction, respectively, while they would be 11.57% and 18.56% in the SSP5-8.5 scenario (Fig. 4e). The rising proportion of warm SSTs in the western or central Pacific means that droughts in the Hanjiang River and even synergistic droughts will be more frequent.

Implications for future water resources management

Coinciding droughts in China, the southwestern United States, and Central Chile were extraordinarily rare in the Pacific Rim region during the last 400 years. However, the frequency and magnitude of extreme hydrological events increased significantly during the 20th century/recent period of global warming. There is considerable uncertainty in predicting the future status of water resources in the Pacific Rim region, which depends on interplay between warming-affected evaporative demand, ENSO longitudinal dynamics-dominated precipitation patterns, and regional water consumption[51–55]. Previous studies have found that climate change has several significant influences on the quantity of globally available water resources, and that regional differences due to climate change may be significant but are highly uncertain[56–58]. The new observation detailed here is that linked water resources along the Pacific Rim are affected by ENSO longitudinal dynamics, and hydroclimate reconstructions and CESM ensemble reveal droughts to be exacerbated by anomalous sea surface temperature patterns, although the probabilities are relatively low. The combined effects of prevailing SST patterns and increasing evaporative demand threaten regional water supply and the stability of the food production.

Our results indicate that the variability of Pacific climate can trigger droughts along the Pacific Rim at any time in the future, not just in North and South America. Considering the impact of greenhouse-gas-driven droughts on the Pacific Rim, transfer projects may not solve the problem of water regional resource shortages, but might even increase the scale of drought impacts in the source areas. Increasing climate anomalies and human intervention challenges the prediction of future water resource changes. It is therefore important to improve our understanding and modeling of the influences of climate change on water resources to cope with ongoing anthropogenic warming.

Methods

Tree-ring and runoff data

We collected incremental cores of pine trees (*Pinus tabulaeformis* and *Pinus bungeana*) from eight sites with shallow rocky soils in the Qinling Mountains, central China, from 2010 to 2022 (Supplementary Table 1). After recording the tree-ring widths to the nearest 0.001 mm, individual tree-ring width series were visually cross-dated. First, all tree-ring width series were detrended to remove non-climatic trends and then averaged to produce the eight site chronologies (Supplemental Fig. 1).

Detrending was accomplished by fitting each ring-width series with a cubic smoothing spline with frequency response 0.50 at 2/3 the sample length, followed by division of the measured width by the value of the spline in each year (ratio detrending. The detrended indices were then averaged into site chronologies using a bi-weight mean. No adjustment was made to detrend chronology variance as a function of changing sample size. We use the standard rather than the residual version of chronologies[59]. The expressed population signal[60] (EPS; Supplemental Table 1 and Fig. 2) was used to identify the period of adequate sample size at each site. In addition to the eight individual chronologies, we combined series from all sites into a regional composite chronology covering a longer reliable interval than any of the individual site chronologies. Instrumental runoff data were obtained from the hydrological station at the Danjiangkou dam site for 1955–2014 (32°31′ N, 111°31′ E, Fig. 1) and used to determine appropriate runoff reconstruction models. The soil moisture reconstruction for the southwestern United States was performed using 1521 tree-ring chronologies, based on the ensemble reconstructions since 800 CE[5]. The PDSI reconstruction for Central Chile is derived from the South American Drought Atlas (SADA) constructed on the basis of 286 tree-ring sites, which was computed using nested Point-by-point regression (PPR), also spanning the last 600 years[25]. Additionally, to identify large-scale forcing of hydroclimate variations in the Hanjiang Basin, the southwestern United States[5], and Central Chile[25], spatial correlation fields for the hydroclimate reconstruction and actual August–July climate (temperature, precipitation, PDSI)[38,61], and runoff[39] were generated.

Runoff reconstructions

The first principal component of a principal component analysis accounted for 46.3–56.7% of the variance of the eight site chronologies for their common period, indicating that pine tree growth responded to a common driving factor (Supplementary Table 2). Significant ($p < 0.05$) correlations with the gridded precipitation ($r = 0.67$), runoff ($r = 0.51$), and temperature ($r = -0.41$) data indicate that pine tree growth is primarily moisture limited. The strongest correlations were found between the tree-ring chronologies and total August–July runoff (Supplementary Fig. 4). The reconstructions were developed using a nested principal component regression procedure[62] and included four separate nests linked continuously from 1620 to 2022 CE (Supplementary Table 2). The reconstruction model was simple linear regression, with runoff as the predictand. For nests beginning 1620 or later, the predictor was the first principal component of the available site chronologies. For the earliest reconstruction interval, 1580-1619, the predictor was the composite regional chronology. The amount of variance explained by the reconstruction is 40.7–44.8%.

Split-sample (first and second halves of 1955–2014) validation was conducted to check the statistical fidelity of the reconstruction models (Supplementary Fig. 2 and Table 2). For each nested subset, the error reduction (RE) and the validation R^2 values were used to assess the skill of each nested model[63]. The final model used for reconstruction was then calibrated using the full instrumental period 1955–2014. The lowest RE and R^2 for the validation period are 0.26 and 0.3 ($n = 30$, $p < 0.01$), respectively, which satisfy the criteria. Because the site chronologies were more up to date than the instrumental runoff record, the reconstructions could extend the instrumental calibration runoff data forwards to 2022. We investigated the occurrence of drought and flood signals in our runoff reconstruction using Superposed Epoch Analysis (SEA)[64], based on two different event year lists, using historical documents[35] and instrumental data.

Drought events and drivers explored

In order to be as revealing as possible about drought variability, we define years below the mean as drought years (Supplementary Table 4). For the drought composites (Fig. 3a, b and Supplementary Figs. 7 and 8), we used the PDSI and SST anomalies from the Paleo Hydrodynamics Data Assimilation product (PHYDA)[12,40].

To reveal the linkages with atmosphere circulations, composite maps of SST, rainfall, and 850 hPa water vapor transport anomalies were produced using the simulated data from the Community Earth System Model Last Millennium Ensemble (CESM-LME)[65]. The CESM1.1 model, employed in CESM-LME simulations, represents a comprehensive tool for simulating Earth's climate system interactions, integrating atmospheric, oceanic, land, and cryosphere processes[66]. The CESM-LME simulations account for the dynamic interplay of initial conditions, external forcings, and physical laws, which may lead to variability in hydroclimate evolutions due to the complex and random nature of internal climate variations. Nonetheless, the model is still based on the fundamental physical laws that control climate processes, allowing us to understand how complex behaviors emerge from basic physical properties and interactions[65–68]. The CESM-LME simulations, as an extensive paleo-hydroclimatic ensemble spanning millennia, provide valuable insights into long-term hydroclimatic drivers, including the Pacific Rim[41,69–71].

Here, the ENSO Longitude Index (ELI)[42,43] is used to indicate changes in ENSO's longitudinal dynamics. The ELI is calculated by first estimating the central Pacific mean SST at each longitude within 5°S-5°N, and subsequently averaged over all longitudes above the mean SST. In this study, the longitude ranges are selected from 170° to 280° and are calculated in every 5°. The smaller the ELI value, the more westward the El Niño occurs. In addition to the spatial correlation with HadISST[72], the main explorations in this study are water vapor transport, runoff distribution, etc. under low and medium ELI conditions.

The probability of at least one of the other two regions (southwestern United States and Central Chile) experiencing drought under Hanjiang River drought conditions is calculated, serving to reveal the risks of synergistic drought occurrences at different time periods. Here, we employed first-order differencing on the data to mitigate the influence of long-term trends and cyclical patterns, enabling a clearer analysis of the data's intrinsic variations and enhancing the accuracy of our probability assessments. Meanwhile, we present the probabilities of west and central El Niño occurrences within the broader context of El Niño events, highlighting their potential impact on drought conditions in the Hanjiang River Basin, or even synergistic drought emergence.

Downscaled and bias-corrected CMIP6 data

We have also extracted the total runoff parameter output of the Hanjiang River Basin, the southwestern United States, and Central Chile from a 24-model ensemble of CMIP6[73]. CMIP6 consists of historical simulations during the period of 1850–2014 and different scenario simulations during the period of 2015–2100. Based on the length of the reconstruction, the period up to 2022 is defined as the historical period, while the period of 2023–2100 is defined as the future period, and the representative SSP2-4.5 and SSP5-8.5 scenarios were used for the future simulation period.

In order to make finer and more realistic predictions, we have performed dynamic downscaling and bias correction on the CMIP6 data[74]. The method begins by regridding the GRUN and CMIP6 data to a horizontal grid spacing of 0.5° × 0.5° using bilinear interpolation. We have then evaluated the performance of all models compared to global runoff dataset[39] (GRUN) for the period 1902–2014, and selected CESM2-WACCM for subsequent analysis (Supplementary Fig. 12). Downscaling and bias correction methods applied to monthly data since 1902, and the GRUN and CMIP6 ensemble data can be decomposed into a long-term nonlinear trend (NLT) plus a perturbation term:

$$GRUN = GRUN_{NLT} + GRUN' \tag{1}$$

$$CMIP6 = CMIP6_{NLT} + CMIP6' \tag{2}$$

The ensemble empirical model decomposition (EEMD) method[75] is used to compute the NLT. Here it is assumed that the variance bias remains constant from the historical period to the future period, so the inclusion of the scaling factor r_s corrects for the bias, while the exclusion of the long-term NLT in the perturbation avoids undue correction.

$$CMIP6'_v = CMIP6' \times r_s \tag{3}$$

where $r_s = SD_{GRUN}/SD_{CMIP6}$, which is the ratio of the standard deviations of the de-trended GRUN and CMIP6 data. The corrected CMIP6 data is then rewritten as:

$$CMIP6_d = GRUN_{NLT} + CMIP6'_v \quad (4)$$

Similarly, future projections will be downscaled and bias corrected according to CESM2-WACCM. Note that climate models may also overestimate or underestimate the magnitude of interannual variability, and thus need to be corrected again for variance bias in future projections based on observed data[74].

In particular, the simulated Hanjiang River runoff was scaled to the same standard deviation and mean values as the observed runoff for our reconstruction models (gaged river discharge volume in m^3/year) enabling us to directly compare the predicted future changes with the reconstruction and observations[76–79]. We assessed the kernel probability density estimation of observed, reconstructed, and simulated runoff data based on a Gaussian distribution, showing great consistency, especially between observed and simulated data (Supplementary Fig. 14a). Instead, the reconstructed data are more centrally normally distributed with a smaller distribution amplitude, revealing a bias in the fit to the extremes[80,81]

Data availability
The runoff reconstruction of Hanjiang River can be downloaded from the Mendeley Data Repository Center (https://doi.org/10.17632/pksym6cjfg.2). The PHYDA dataset is archived at https://zenodo.org/record/1198817. The CESM-LME datasets were provided from https://www.earthsystemgrid.org/dataset/ucar.cgd.ccsm4.CESM_CAM5_LME.html. The CMIP6 datasets are accessible at https://esgf-node.llnl.gov/search/cmip6/. The observation gridded datasets (CRU, GRUN, and HadISST) can be obtained from http://climexp.knmi.nl/.

Code availability
The code to perform these analyses is available from the corresponding authors upon request.

Received: 20 February 2024; Accepted: 21 June 2024;
Published online: 29 June 2024

References
1. Barnett, J., Rogers, S., Webber, M., Finlayson, B. & Wang, M. Sustainability: transfer project cannot meet China's water needs. *Nature* **527**, 295–297 (2015).
2. Zhao, X. et al. Physical and virtual water transfers for regional water stress alleviation in China. *Proc. Natl Acad. Sci. USA* **112**, 1031–1035 (2015).
3. Brown, T. C., Mahat, V. & Ramirez, J. A. Adaptation to future water shortages in the United States caused by population growth and climate change. *Earth Future* **7**, 219–234 (2019).
4. Shumilova, O., Tockner, K., Thieme, M., Koska, A. & Zarfl, C. Global water transfer megaprojects: a potential solution for the water-food-energy nexus? *Front. Environ. Sci.* **6**, 150 (2018).
5. Williams, A. P. et al. Large contribution from anthropogenic warming to an emerging North American megadrought. *Science* **368**, 314–318 (2020).
6. Woodhouse, C. A. et al. Upper Colorado River Basin 20th century droughts under 21st century warming: plausible scenarios for the future. *Clim. Serv.* **21**, 100206 (2021).
7. Liu, X. M., Liu, C. M., Luo, Y. Z., Zhang, M. H. & Xia, J. Dramatic decrease in streamflow from the headwater source in the central route of China's water diversion project: climatic variation or human influence? *J. Geophys. Res. -Atmos.* **117**, D06113 (2012).
8. Qi, B. Y., Liu, H. H., Zhao, S. F. & Liu, B. Y. Observed precipitation pattern changes and potential runoff generation capacity from 1961–2016 in the upper reaches of the Hanjiang River Basin, China. *Atmos. Res.* **254**, 105392 (2021).
9. Ma, M. et al. The 2022 extreme drought in the Yangtze River Basin: characteristics, causes and response strategies. *River* **1**, 162–171 (2022).
10. Wang, H., Sun, F. B. & Liu, W. B. Characteristics of streamflow in the main stream of Changjiang River and the impact of the Three Gorges Dam. *Catena* **189**, 104498 (2020).
11. Williams, A. P., Cook, B. I. & Smerdon, J. E. Rapid intensification of the emerging southwestern North American megadrought in 2020–2021. *Nat. Clim. Change* **12**, 232–234 (2022).
12. Steiger, N. J., Smerdon, J. E., Seager, R., Williams, A. P. & Varuolo-Clarke, A. M. ENSO-driven coupled megadroughts in North and South America over the last millennium. *Nat. Geosci.* **14**, 739–744 (2021).
13. Garreaud, R. D. et al. The central Chile mega drought (2010-2018): a climate dynamics perspective. *Int. J. Climatol.* **40**, 421–439 (2020).
14. Fuentealba, M., Bahamóndez, C., Sarricolea, P., Meseguer-Ruiz, O. & Latorre, C. The 2010–2020 'megadrought' drives reduction in lake surface area in the Andes of central Chile (32°-36° S). *J. Hydrol. -Reg. Stud.* **38**, 100952 (2021).
15. Liu, P. W. et al. Groundwater depletion in california's central valley accelerates during megadrought. *Nat. Commun.* **13**, 7825 (2022).
16. Woodhouse, C. A., Meko, D. M. & Bigio, E. R. A long view of Southern California water supply: perfect droughts revisited. *J. Am. Water Resour. Assoc.* **56**, 212–229 (2020).
17. Xiao, M., Udall, B. & Lettenmaier, D. P. On the causes of declining Colorado River streamflows. *Water Resour. Res.* **54**, 6739–6756 (2018).
18. Venegas-González, A. et al. Sclerophyllous Forest tree growth under the influence of a historic megadrought in the mediterranean ecoregion of Chile. *Ecosystems* **26**, 344–361 (2022).
19. González, M. E., Gómez-González, S., Lara, A. & Garreaud, R. & Díaz-Hormazábal, I. The 2010–2015 Megadrought and its influence on the fire regime in central and south-central Chile. *Ecosphere* **9**, e02300 (2018).
20. Kannenberg, S. A., Driscoll, A. W., Szejner, P., Anderegg, W. R. & Ehleringer, J. R. Rapid increases in shrubland and forest intrinsic water-use efficiency during an ongoing megadrought. *Proc. Natl Acad. Sci. USA* **118**, e2118052118 (2021).
21. Williams, A. P. et al. Observed impacts of anthropogenic climate change on wildfire in California. *Earth Future* **7**, 892–910 (2019).
22. Hassrick, J. L., Ammann, A. J., Perry, R. W., John, S. N. & Daniels, M. E. Factors Affecting spatiotemporal variation in survival of endangered Winter-Run Chinook Salmon Out-migrating from the Sacramento River. *North Am. J. Fish. Manag.* **42**, 375–395 (2022).
23. Stevenson, S., Timmermann, A., Chikamoto, Y., Langford, S. & DiNezio, P. Stochastically generated north American megadroughts. *J. Clim.* **28**, 1865–1880 (2015).
24. Cook, E. R. et al. Asian monsoon failure and megadrought during the last millennium. *Science* **328**, 486–489 (2010).
25. Morales, M. S. et al. Six hundred years of South American tree rings reveal an increase in severe hydroclimatic events since mid-20th century. *Proc. Natl Acad. Sci. USA* **117**, 16816–16823 (2020).
26. Ho, M., Lall, U., Sun, X. & Cook, E. R. Multiscale temporal variability and regional patterns in 555 years of conterminous US streamflow. *Water Resour. Res.* **53**, 3047–3066 (2017).
27. Urrutia, R. B. et al. Multicentury tree ring reconstruction of annual streamflow for the Maule River watershed in south central Chile. *Water Resour. Res.* **47**, W06527 (2011).
28. Barria, P., Peel, M. C., Walsh, K. J. E. & Muñoz, A. The first 300-year streamflow reconstruction of a high-elevation river in Chile using tree rings. *Int. J. Climatol.* **38**, 436–451 (2018).
29. Woodhouse, C. A. & Lukas, J. J. Multi-century tree-ring reconstructions of Colorado streamflow for water resource planning. *Clim. Change* **78**, 293–315 (2006).

30. Woodhouse, C. A., Stahle, D. W. & Díaz, J. V. Rio Grande and Rio Conchos water supply variability over the past 500 years. *Clim. Res.* **51**, 147–158 (2012).
31. Meko, D. M. & Woodhouse, C. A. Tree-ring footprint of joint hydrologic drought in Sacramento and Upper Colorado river basins, western USA. *J. Hydrol.* **308**, 196–213 (2005).
32. Cook, E. R. et al. Old World megadroughts and pluvials during the Common Era. *Sci. Adv.* **1**, e1500561 (2015).
33. Xu, C. X. et al. Increased variability of Thailand's Chao Phraya River peak season flow and its association with ENSO variability: Evidence from tree ring $\delta^{18}O$. *Geophys. Res. Lett.* **46**, 4863–4872 (2019).
34. Chen, F. et al. Coupled Pacific Rim megadroughts contributed to the fall of the Ming Dynasty's capital in 1644 CE. *Sci. Bull*. https://doi.org/10.1016/j.scib.2024.04.029 (2024).
35. Yuan, L. *The Northwestern Drought and History of the Famine* (The Gansu People's Press, 1994).
36. Li, X. et al. Changes in precipitation extremes in the Yangtze River Basin during 1960–2019 and the association with global warming, ENSO, and local effects. *Sci. Total Environ.* **760**, 144244 (2021).
37. Cai, W. et al. Analysis of climate change in the middle reaches of the Yangtze River Basin using principal component analysis. *Theor. Appl. Climatol.* **151**, 449–465 (2022).
38. van der Schrier, G., Barichivich, J., Briffa, K. R. & Jones, P. D. A scPDSI-based global data set of dry and wet spells for 1901-2009. *J. Geophys. Res. -Atmos.* **118**, 4025–4048 (2013).
39. Ghiggi, G., Humphrey, V., Seneviratne, S. I. & Gudmundsson, L. G-RUN ENSEMBLE: a multi-forcing observation-based global runoff reanalysis. *Water Resour. Res.* **57**, e2020WR028787 (2021).
40. Steiger, N. J., Smerdon, J. E., Cook, E. R. & Cook, B. I. Data Descriptor: a reconstruction of global hydroclimate and dynamical variables over the Common Era. *Sci. Data* **5**, 180086 (2018).
41. Hessl, A. E. et al. Past and future drought in Mongolia. *Sci. Adv.* **4**, e1701832 (2018).
42. Williams, I. N. & Patricola, C. M. Diversity of ENSO events unified by convective threshold sea surface temperature: a nonlinear ENSO index. *Geophys. Res. Lett.* **45**, 9236–9244 (2018).
43. Patricola, C. M. et al. Maximizing ENSO as a source of western US hydroclimate predictability. *Clim. Dyn.* **54**, 351–372 (2020).
44. England, M. H. et al. Recent intensification of wind-driven circulation in the Pacific and the ongoing warming hiatus. *Nat. Clim. Change* **4**, 222–227 (2014).
45. Meng, Q. J. et al. Twentieth century Walker Circulation change: data analysis and model experiments. *Clim. Dyn.* **38**, 1757–1773 (2012).
46. Zhang, L. & Li, T. Relative roles of differential SST warming, uniform SST warming and land surface warming in determining the Walker circulation changes under global warming. *Clim. Dyn.* **48**, 987–997 (2017).
47. Wu, M. N. et al. A very likely weakening of Pacific Walker Circulation in constrained near-future projections. *Nat. Commun.* **12**, 6502 (2021).
48. Rehbein, A. & Ambrizzi, T. ENSO teleconnections pathways in South America. *Clim. Dyn.* **61**, 1277–1292 (2023).
49. Tedeschi, R. G., Grimm, A. M. & Cavalcanti, I. F. A. Influence of Central and East ENSO on precipitation and its extreme events in South America during austral autumn and winter. *Int. J. Climatol.* **36**, 4797–4814 (2016).
50. Wu, R. G. & Zhang, L. Biennial relationship of rainfall variability between Central America and equatorial South America. *Geophys. Res. Lett.* **37**, L08701 (2010).
51. Milly, P. C. & Dunne, K. A. Colorado River flow dwindles as warming-driven loss of reflective snow energizes evaporation. *Science* **367**, 1252–1255 (2020).
52. Yang, Y. M., Park, J. H., An, S. I., Wang, B. & Luo, X. Mean sea surface temperature changes influence ENSO-related precipitation changes in the mid-latitudes. *Nat. Commun.* **12**, 1495 (2021).
53. Xu, L. et al. Potential precipitation predictability decreases under future warming. *Geophys. Res. Lett.* **47**, e2020GL090798 (2020).
54. Viviroli, D., Kummu, M., Meybeck, M., Kallio, M. & Wada, Y. Increasing dependence of lowland populations on mountain water resources. *Nat. Sustain.* **3**, 917–928 (2020).
55. Dolan, F. et al. Evaluating the economic impact of water scarcity in a changing world. *Nat. Commun.* **12**, 1915 (2021).
56. He, C. Y. et al. Future global urban water scarcity and potential solutions. *Nat. Commun.* **12**, 4667 (2021).
57. Pokhrel, Y. et al. Global terrestrial water storage and drought severity under climate change. *Nat. Clim. Chang.* **11**, 226–233 (2021).
58. Konapala, G., Mishra, A. K., Wada, Y. & Mann, M. E. Climate change will affect global water availability through compounding changes in seasonal precipitation and evaporation. *Nat. Commun.* **11**, 3044 (2020).
59. Cook, E. R. & Kairiukstis, L. A. (eds.). *Methods of Dendrochronology: Ap-plications in the Environmental Sciences* (Kluwer Academic Publishers, 1990).
60. Wigley, T. M. L., Briffa, K. R. & Jones, P. D. On the average value of correlated time series, with applications in dendroclimatology and hydrometeorology. *J. Clim. Appl. Meteorol.* **23**, 201–213 (1984).
61. Harris, I., Jones, P. D., Osborn, T. J. & Lister, D. H. Updated high-resolution grids of monthly climatic observations-the CRU TS3. 10 Dataset. *Int. J. Climatol.* **34**, 623–642 (2014).
62. Meko, D. Dendroclimatic reconstruction with time varying predictor subsets of tree indices. *J. Clim.* **10**, 687–696 (1997).
63. Fritts, H. C. *Tree Rings and Climate* (Academic Press, 1976).
64. Haurwitz, M. W. & Brier, G. W. A critique of the superposed epoch analysis method: its application to solar–weather relations. *Mon. Weather Rev.* **109**, 2074–2079 (1981).
65. Otto-Bliesner, B. L. et al. Climate variability and change since 850 CE: An ensemble approach with the Community Earth System Model. *Bull. Am. Meteorol. Soc.* **97**, 735–754 (2016).
66. Hurrell, J. W. et al. The Community Earth System Model: a framework for collaborative research. *Bull. Am. Meteorol. Soc.* **94**, 1339–1360 (2013).
67. Blackmon, M. et al. The community climate system model. *Bull. Am. Meteorol. Soc.* **82**, 2357–2376 (2001).
68. Davis, N. A. et al. Climate, variability, and climate sensitivity of "middle atmosphere" chemistry configurations of the community earth system model version 2, whole atmosphere community climate model version 6 (CESM2(WACCM6)). *J. Adv. Model. Earth Syst.* **15**, e2022MS003579 (2023).
69. Stevenson, S., Otto-Bliesner, B., Fasullo, J. & Brady, E. "El Nino Like" hydroclimate responses to last millennium volcanic eruptions. *J. Clim.* **29**, 2907–2921 (2016).
70. Roldán-Gómez, P. J., González-Rouco, J. F., Smerdon, J. E. & García-Pereira, F. Model and proxy evidence for coordinated changes in the hydroclimate of distant regions over the Last Millennium. *Clim. Past* **19**, 2361–2387 (2023).
71. Xue, J. et al. The combined influences of Solar Radiation and PDO on Precipitation over Eastern China during the last millennium. *Clim. Dyn.* **60**, 1137–1150 (2023).
72. Rayner, N. A. et al. Global analyses of sea surface temperature, sea ice, and night marine air temperature since the late nineteenth century. *J. Geophys. Res. -Atmos.* **108**, 4407 (2003).
73. Eyring, V. et al. Overview of the Coupled Model Intercomparison Project Phase 6 (CMIP6) experimental design and organization. *Geosci. Model Dev.* **9**, 1937–1958 (2016).
74. Xu, Z. F., Han, Y., Tam, C. Y., Yang, Z. L. & Fu, C. B. Bias-corrected CMIP6 global dataset for dynamical downscaling of the historical and future climate (1979-2100). *Sci. Data* **8**, 293 (2021).
75. Wu, Z. & Huang, N. E. Ensemble Empirical Mode Decomposition: a noise-assisted data analysis method. *Adv. Adapt. Data Anal.* **1**, 1–41 (2009).

76. Rao, M. P. et al. Seven centuries of reconstructed Brahmaputra River discharge demonstrate underestimated high discharge and flood hazard frequency. *Nat. Commun.* **11**, 6017 (2020).
77. Chen, F. et al. Southeast Asian ecological dependency on Tibetan Plateau streamflow over the last millennium. *Nat. Geosci.* **16**, 1151–1158 (2023).
78. Zhao, X. E., Fang, K. Y., Chen, F., Martín, H. & Roig, F. A. Reconstructed Jing River streamflow from western China: a 399-year perspective for hydrological changes in the Loess Plateau. *J. Hydrol.* **621**, 129573 (2023).
79. Yue, W. P. et al. *Picea schrenkiana* tree ring blue intensity reveal recent glacier mass loss in High Mountain Asia is unprecedented within the last four centuries. *Global Planet. Change* **604**, 111211 (2023).
80. Chen, F. et al. Ecological and societal effects of Central Asian streamflow variation over the past eight centuries. *npj Clima. Atmos. Sci.* **5**, 21 (2022).
81. Wang, S. J. et al. Reconstructed springtime (March-June) precipitation tracked by tree rings dating back to 1760 CE in the Qinling-Bashan mountainous area. *Paleogeogr. Paleoclimatol. Paleoecol.* **604**, 111211 (2022).

Acknowledgements
This work was supported by NSFC (41988101, 32061123008). J.E. and U.B. would like to acknowledge the support of the ERC Advanced project entitled Monostar (AdG 882727).

Author contributions
F.C., S.W., Q.D., T.W., W.Y., X.Z., and F.H.C. developed the original research design and collected and analyzed the historical documentary data. F.C., U.B., J.E., D.M., H.L., M.H., A.G., and F.H.C. wrote the article together and made the interpretations together. All authors reviewed the final manuscript.

Competing interests
The authors declare no competing interests.

Additional information
Supplementary information The online version contains supplementary material available at https://doi.org/10.1038/s41612-024-00706-1.

Correspondence and requests for materials should be addressed to Feng Chen.